COMPUTATIONAL FLUID DYNAMICS SIMULATIONS OF INSPIRATORY AIRFLOW IN THE HUMAN NOSE AND NASOPHARYNX

Ravi P. Subramaniam, Regina B. Richardson, Kevin T. Morgan, Julia S. Kimbell

Chemical Industry Institute of Toxicology, Research Triangle Park, North Carolina, USA

Raymond A. Guilmette

Lovelace Respiratory Research Institute, Albuquerque, New Mexico, USA

Extrapolation of the regional dose of an inhaled xenobiotic from laboratory animals to humans for purposes of assessing human health risk is problematic because of large interspecies differences in nasal respiratory physiology and airway anatomy. There is a need for dosimetry models that can adjust for these differences in the upper respiratory tract. The present work extends previous efforts in this laboratory and elsewhere to simulate nasal airflow profiles numerically in laboratory animals and humans. A three-dimensional, anatomically accurate representation of an adult human nasal cavity and nasopharynx was constructed. The Navier–Stokes and continuity equations for airflow were solved using the finite-element method under steady-state, inspiratory conditions simulating rest and light exercise (steady-state inspiratory flow rates: 15 L/min and 26 L/min, respectively) with the fluid dynamics software package FIDAP. Simulated airflow was streamlined in the main nasal passages and complex in the vestibule and nasopharynx. Swirling air currents and recirculating flow were predicted in the nasal vestibule, and the expansion at the nasopharynx gave rise to two downward, countercurrent, spiraling vortices. Significant lateral flow was observed mainly in the middle lateral meatus. Flow apportionment among different regions of the nose remained almost unchanged between the two inspiratory rates simulated. Fastest flow occurred in the posterior nasal valve region. In the main nasal airway, the highest airspeeds occurred through the ventral and middle medial regions. Simulated velocity fields and pressure drops across the nasal cavity generally agreed with experimental results from the literature. It is proposed that this model can be used to reduce uncertainty in human health risk assessment for inhaled materials and to assess changes in airflow and nasal resistance due to common surgical procedures and medical conditions.

Received 14 June 1997; accepted 8 September 1997.

The authors thank Drs. Grace Kepler, Rory Conolly, Fred Miller, Bahman Asgharian, and Clay Frederick for useful discussions and suggestions, Dr. Matt Godo for continued assistance in the use of FIDAP, Donald Joyner for assistance with the graphics, and Dr. Barbara Kuyper for her careful editing of the manuscript. This work was partly carried out using computational resources at the North Carolina Supercomputer Center. The research described in this work has been funded in part by the Environmental Criteria and Assessment Office, the U.S. Environmental Protection Agency, under assistance number CR820429 to CIIT. However, it has not been subjected to the agency's peer and administrative review and therefore may not necessarily reflect the views of the agency, and no official endorsement should be inferred.

Current address for Kevin T. Morgan is Glaxo-Wellcome, Inc., Research Triangle Park, NC, USA.

Address correspondence to Dr. Ravi P. Subramaniam, CIIT, PO Box 12137, Research Triangle Park, NC 27709, USA. E-mail: ravi@ciit.org.

Inhalation Toxicology, 10:91–120, 1998
Copyright © 1998 Taylor & Francis
0895–8378/98 $12.00 + .00

RIGHTSLINK

Inhalation Toxicology Downloaded from informahealthcare.com by University of Waterloo on 12/12/14
For personal use only.

Inhalation Toxicology Downloaded from informahealthcare.com by University of Waterloo on 12/12/14
For personal use only.

Knowledge of airflow in the human nose is important for understanding many aspects of the biology and pathology of the respiratory tract. The nasal passages absorb a significant proportion of many gases and particles from inhaled air prior to its delivery to the lower respiratory tract (Andersen & Proctor, 1982). While this filtration protects the lower respiratory tract, it also makes the upper respiratory tract vulnerable to the deleterious effects of xenobiotics. Studies in laboratory animals have demonstrated that nasal lesions induced by exposure to many inhaled gases form in species-specific patterns (Morgan & Monticello, 1990). Olsen and Asnaes (1985) and Roush et al. (1987) have implicated the human nasopharynx as a target site for the occurrence of nasal cancer; the nearly right-angled bend of the airway at this point makes the nasopharynx particularly vulnerable to effects of airborne toxicants. Patterns of upper respiratory airflow are thought to play a major role in determining tissue dose associated with these lesion distributions (Morgan & Monticello, 1990). To develop a model that can predict regional tissue dose for inhaled air pollutants in humans, detailed information about human nasal airflow patterns is needed.

Airflow profiles in human nasal passages have been studied experimentally by a number of researchers (e.g., Girardin et al., 1983; Hahn et al., 1993; Masing, 1967; Proetz, 1951; Hornung et al., 1987; Swift & Proctor, 1977). These studies provide valuable descriptions of airflow patterns in the nasal passages of different individuals; however, quantitative information about the airflow is limited. Hahn et al. (1993) provided experimentally measured velocity information on five cross sections of the nasal mold. Airflow information throughout the nose is needed to predict regional transport of inhaled material, and this information can be provided by numerical simulation of nasal airflow.

Numerical studies using realistic nasal geometries have not been possible until recent advances in both computer hardware and software. Numerical simulations of human nasal airflow have been conducted by Elad et al. (1993), Tarabichi and Fanous (1993), and Keyhani et al. (1995), the last being the most detailed of these studies. In their numerical work, Keyhani et al. (1995) examined airflow through one side of the human nose in a three-dimensional model that was truncated anterior to the nasopharynx. The purpose of the work presented here was (1) to extend these studies by using computational fluid dynamics (CFD) simulations to predict the nasal airflow field for steady-state inspiration in an anatomically accurate computer reconstruction of both sides of the human nasal passages that included the posterior nasal airway and nasopharynx and (2) to compare simulated velocity profiles with experimental results described by Hahn et al. (1993). The flow profile was correlated with nasal anatomy, which plays an important role in determining nasal resistance to flow. We studied flow in the nasal vestibule and in the naso-

RIGHTSLINK

pharynx in particular detail, since the airflow profiles in these regions have hitherto not been well investigated.

The human airflow model presented here provides data that can be used as input to computational models that address site-specific uptake of chemicals and deposition of particles in the nasal passages (e.g., Subramaniam et al., 1996; Kimbell et al., 1993; Frederick et al., 1994). The computer reconstruction may be modified to reflect common surgical and medical conditions. Thus the model can also be used to identify potential subpopulations that may receive higher regional doses of inhaled material in their upper respiratory tracts than the general population.

Inhalation Toxicology Downloaded from informahealthcare.com by University of Waterloo on 12/12/14
For personal use only.

NASAL ANATOMY

The nasal passages have a complex geometry (Negus, 1958). A lateral outline of the human nasal passages with various sections labeled is shown in Figure 1. We assume a standing position in this discussion of the nasal anatomy and in our simulations. The anterior three-fourths of the nose is divided into two enantiomorphic parts by the nasal septum. Entrance to these two cavities is through the external nares, or nostrils, which are slightly slanted with respect to the hard palate. The nasal vestibule is a funnel-shaped region extending about 1.5 cm from the anterior tip of the nose and includes the nostril section. The vestibule leads to the constricted nasal valve region, the posterior boundary of which is roughly presumed to be the anterior limit of the inferior turbinate (Proctor, 1982). The nasal valve, which has been conventionally defined as the site of narrowest cross-sectional area of the nasal passage posterior to the nostril opening, accounts for more than half of the total nasal resistance (Haight & Cole, 1983). The exact location and orientation of the nasal valve have been matters of some controversy (Cole, 1993). In this article, we follow the tradition of other authors (Proctor, 1982; Lanza & Clerico, 1995) in referring broadly to the nasal valve region. The nasal vestibule and valve region form a flow-limiting structure that is collapsible when the pressure difference between the ambient and the respired air in this portion of the airway exceeds a critical value. This collapse occurs when inspiratory rates exceed about 45 L/min (Bridger & Proctor, 1970, Figure 3), which are much greater than those considered in this study. Such a collapse was therefore not incorporated into our model, which assumes the boundary of the nasal airway to be rigid throughout. In contrast with this rigid characterization, the nasal airway is, in reality, a dynamically changing structure. Most individuals demonstrate a coordinated nasal cycle where the nasal passages on one side of the nose are occluded to various degrees due to tissue congestion for a certain period of time (Cole, 1982). This physiological effect will lead to dynami-

RIGHTSLINK

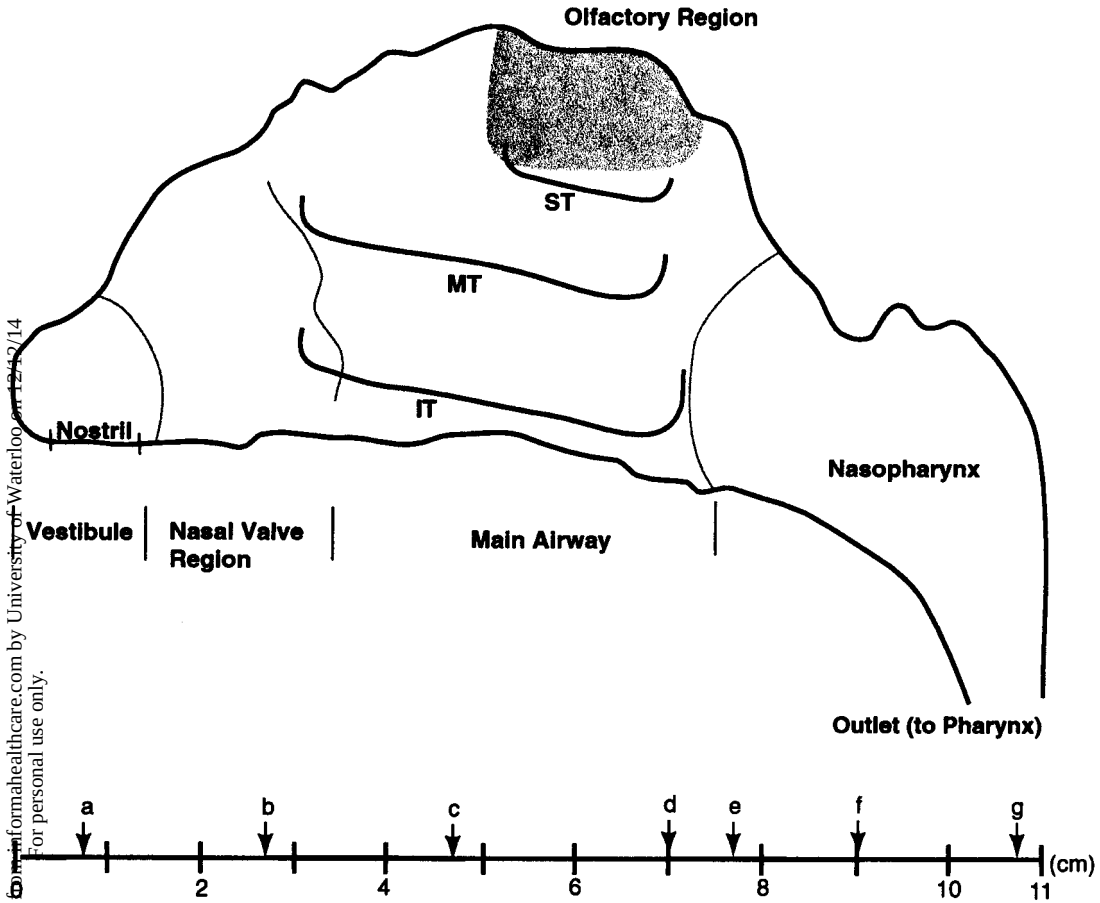

FIGURE 1. Lateral view of the left human nose. Labels a–g mark locations of the coronal sections in Figure 2A. The shaded area marks the olfactory region. The gray lines mark anteroposteriorly the posterior boundaries of the vestibule and nasal valve region and the anterior boundary of the nasopharynx. ST, MT, and IT refer to the superior, middle, and inferior turbinates. The boundaries of the olfactory region are as depicted in Lang (1989) and those of the vestibular, nasal valve, and nasopharyngeal regions are as illustrated by Proctor (1982).

cally changing differences in the airflow profiles on the two sides of the nose.

At the constriction around the nasal valve region, the airway undergoes a right-angled bend toward the nasal floor, with a sudden increase in the coronal cross-sectional area of the passages (Proctor, 1982). As a consequence, airflow in humans has been reported to become turbulent in this region (Cole, 1982). The region between the nasal valve region and the nasopharynx is referred to as the main nasal airway. Coronal cross sections of the nasal passage are dramatically different in shape at various distances along the long axis of the nose (as seen in Figure 2A)

Inhalation Toxicology Downloaded from informahealthcare.com by University of Waterloo on 12/13/14
For personal use only.

RIGHTSLINK

Inhalation Toxicology Downloaded from informahealthcare.com by University of Waterloo on 12/12/14
For personal use only.

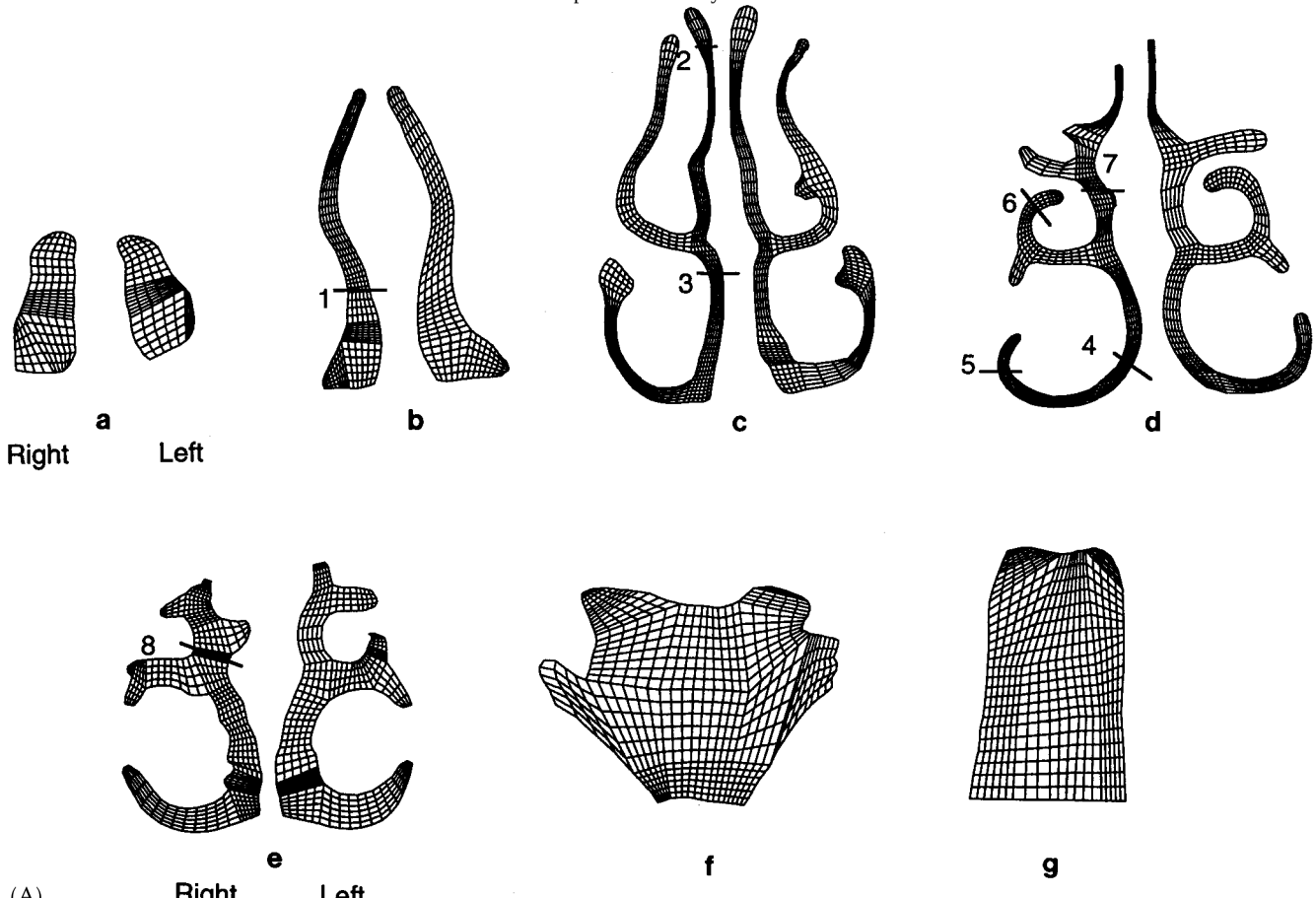

FIGURE 2. (A) Representative coronal sections whose positions are marked in Figure 1. Parts b–e are sections on which experimental and simulated velocities are compared, with solid lines indicating the locations across the airway at which the measurements were made. The label (1–8) by the solid line refers to the corresponding plot in Figure 10.

RIGHTSLINK

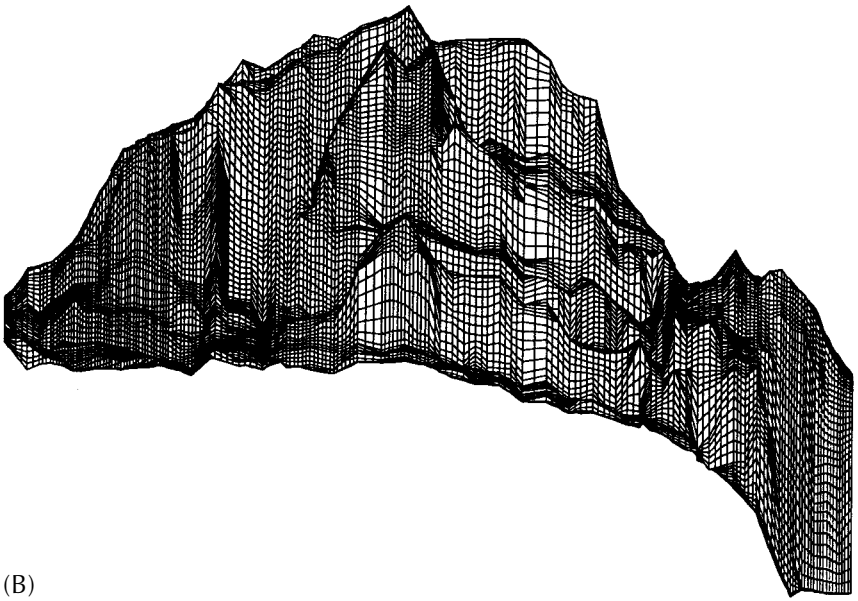

(B)

FIGURE 2. (*Continued*) (B) Lateral view of the three-dimensional finite-element mesh of the nasal cavity.

Inhalation Toxicology Downloaded from informahealthcare.com by University of Waterloo on 12/12/14
For personal use only.

and become increasingly convoluted in the main airway. Three projections on the lateral wall of the nose, known as the inferior, middle, and superior turbinates, lead to a vertical partitioning of the main airway into the three regions shown in Figure 3, namely dorsal, middle, and ventral. The passages are further partitioned horizontally as medial or lateral for the portions adjoining the septum and outer nasal boundary, respectively. The posterior half of the dorsal airway constitutes the olfactory region. The dorsal airway is generally narrow and slit-like. Airflow through this portion of the airway is therefore easily occluded. A plot of coronal cross-sectional area versus axial distance from the anterior limit of the nose is shown in Figure 4.

The two nasal passages join to form a single passage at the posterior end of the septum. This fusion takes place at the posterior end of the inferior turbinate located immediately posterior to coronal section e (see Figures 1 and 2A), and marks the entrance to the nasopharynx. The passages fuse only at the ventral medial boundary of the septum at the anterior nasopharynx; therefore, dorsoventrally nasal passages are low at this location. Such a depression of the nasal roof is followed by a sudden funnel-shaped expansion of the airway in the region between coronal sections e and f of Figure 2A and a change in the direction of the flowstream. While the roof of the nasal cavity is angled upward at about 45 degrees to the plane of the hard palate, the nasal floor undergoes a gradual right-angled

RIGHTSLINK

bend downward. The airways then proceed vertically downward with a roughly uniform circular cross section toward the pharynx.

METHODS

The three-dimensional, finite-element mesh (or grid) used in the calculation (Figure 2B) was developed from magnetic resonance imaging

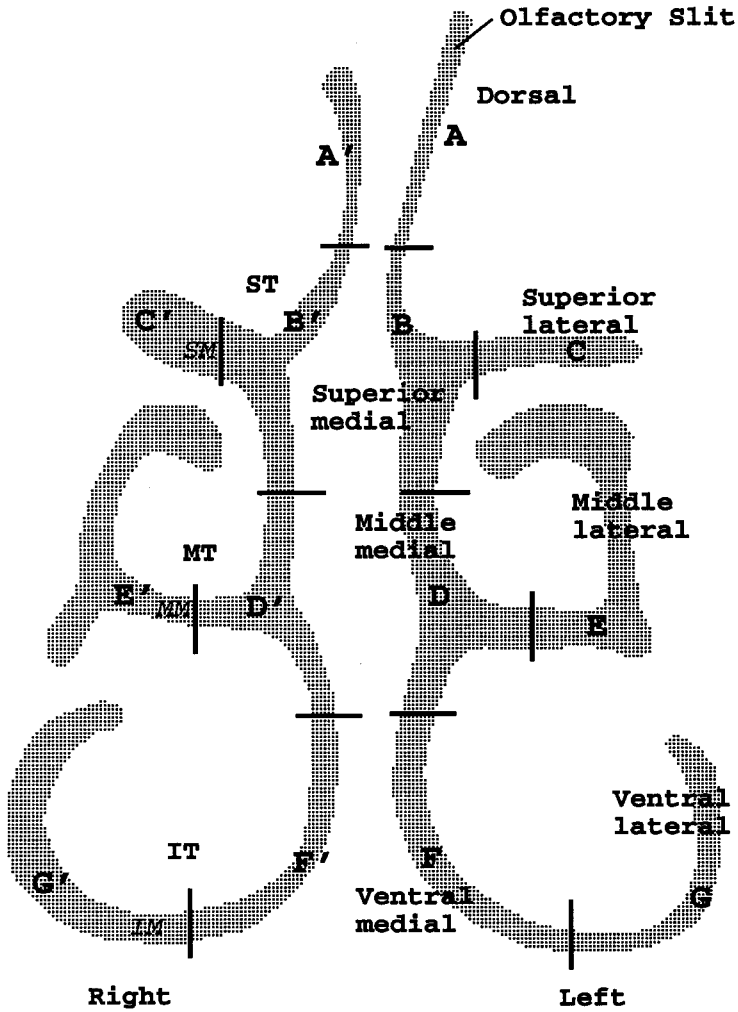

FIGURE 3. Coronal section locating various anatomical structures and airways. The section is located at 6 cm from the anterior tip of the nose. ST, MT, and IT: superior, middle, and inferior turbinate, respectively. SM, MM and IM: superior, middle, and inferior meatus, respectively. Regions A–G and A′–G′ are labeled for use in Tables 1 and 3.

Inhalation Toxicology Downloaded from informahealthcare.com by University of Waterloo on 12/12/14
For personal use only.

RIGHTSLINK

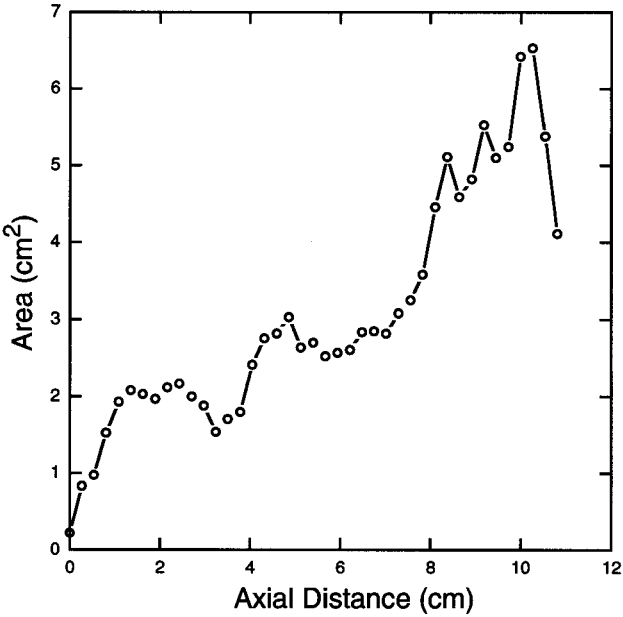

FIGURE 4. Cross-sectional area of coronal sections versus distance from anterior end.

Inhalation Toxicology Downloaded from informahealthcare.com by University of Waterloo on 12/12/14
For personal use only.

(MRI) scans of the nose of a healthy, 53-yr-old, nonsmoking Caucasian male (73 kg mass, 173 cm height) (Guilmette et al., 1994). The scans provided 36 contiguous coronal images of the nose at intervals of 3 mm. Representative coronal slices of different regions of the nose are shown in Figure 2A. The airway perimeters traced from the images were first used to construct two-dimensional, finite-element grids of each coronal slice, which were subsequently linked together to form the three-dimensional, finite-element mesh of the nasal airways. The reconstruction utilized both in-house (Godo et al., 1995) and commercial software (FIDAP, Fluent, Inc., Lebanon, NH). The finite-element model used 130,000 brick elements, comprising 156,000 nodes (shown in Figure 2B). While the main purpose of the reconstruction was to furnish a grid on which the finite-element equations could be solved, the reconstruction also allows the extraction of morphometric information and visualization of the geometric structure of the nasal passages.

The flow of air is described by the Navier–Stokes and continuity equations, which under steady-state conditions are written as

$$\rho u_j \frac{\partial u_i}{\partial x_j} = -\frac{\partial p}{\partial x_i} + \mu \frac{\partial^2 u_i}{\partial x_j \partial x_j}$$

$$\frac{\partial u_j}{\partial x_j} = 0$$

RIGHTSLINK

Indices *i,j* take values 1 to 3, and summation over repeated indices is assumed. The solution variables are the velocity components, u_i (cm/s), and the pressure, p (dyn/cm^2). The terms μ and ρ are the dynamic viscosity (cm^2/s) and mass density of air (g/cm^3), respectively. The inspired air may be considered incompressible at physiologic flow rates (Vogel, 1994). In this work, we considered flow only under steady-state inspiratory conditions. This and other approximations of the model are addressed further in the discussion.

The following conditions were imposed on the spatial boundaries of the flow field:

1. A no-slip condition (fluid velocity = zero) was imposed at the surface of the nasal airway walls.
2. A stress-free condition was established at the outlet. This condition is satisfied if the normal velocity gradients are set to zero at the outlet.
3. At the nostril surface (the flow inlet), plug-flow conditions were specified. These conditions were that the velocity vectors are of uniform length and perpendicular to the surface. While these conditions are an approximation, other simulations of nasal airflow (Keyhani et al., 1995; Kimbell et al., 1993) have shown that the downstream flow field is not altered significantly from that obtained by using more realistic inlet velocity profiles.

We applied the finite-element method (Zienkiewicz, 1977) using the commercial fluid dynamics solution package FIDAP to solve the equations of motion for airflow. The finite-element method obtains solutions to the full Navier–Stokes and continuity equations within each element of the finite-element mesh. We used the pressure projection method of the segregated algorithm within FIDAP to solve the set of nonlinear, finite-element, flow equations. The system of equations is solved in FIDAP using iterative techniques (Fluid Dynamics International, 1991). Details of the solution method have been elucidated by Keyhani et al. (1995). Further details may also be found in the FIDAP *Theory Manual* (Fluid Dynamics International, 1991).

We obtained converged solutions up to the inspiratory volumetric flow rate of 28 L/min, which corresponds to a Reynolds number (ratio of inertial to viscous forces) of 1360 at the nostril. To obtain convergence, the solution was first obtained for a low inspiratory flow rate (4 L/min). This solution was then used as a seed for the subsequent iteration at an increased flow rate. This incremental loading procedure was continued until convergence was obtained at the desired inspiratory flow rate.

The finite-element solution resulted in artificial gradients of the flow variables occurring in some regions of the computational grid. While these artificial gradients were eliminated, wherever possible, by refining and reformulating the mesh, the complexity of the nasal geometry limited

Inhalation Toxicology Downloaded from informahealthcare.com by University of Waterloo on 12/12/14
For personal use only.

RIGHTSLINK

the extent to which the refinement was feasible because of increased requirements on computational resources. Spatial instabilities in the solution arising because of sharp gradients were stabilized by using a hybrid method of streamline and first-order upwinding schemes available in FIDAP (Fluid Dynamics International, 1996). A streamline upwinding factor of 1.0 was used in the simulation results reported here. Dependence of numerical results on coarseness of the finite-element mesh was characterized by comparing airflow speed, pressure, and volumetric flow at various locations for 3 different mesh densities of 156,000, 124,000, and 86,000 nodes, respectively.

Inhalation Toxicology Downloaded from informahealthcare.com by University of Waterloo on 12/12/14
For personal use only.

RESULTS

We first present a qualitative description of the calculated airflow profile by simulating flow streamlines. The flow field is next quantitatively characterized by presenting calculated flow velocities and volumetric flow rates. Finally, the component of air velocity along the axial direction of the nose is compared with experimental observations. The minute volume of air, equal to 7.5 L/min for an adult human male (ICRP, 1975), is a value obtained for bidirectional flow of air through the nose. The steady-state inspiratory flow rate was therefore set equal to twice the value of the minute volume for resting breathing. The flow field is discussed in detail for steady-state inspiration of air at the flow rate of 15 L/min. Results for a higher inspiratory rate of 26 L/min (corresponding to light exercise) are compared with those obtained at 15 L/min when reporting volumetric flow and air velocities. The calculated pressure drop across the nose is compared with measurements made by Schreck et al. (1993) in a laboratory model of the human nose and by Hirschberg et al. (1995) on human subjects.

Flow Stream Patterns

A streamline, which is the path traversed by a massless particle released at a given point in the fluid flow, provides a qualitative visualization of the flow field. The calculated flow streamlines are analogous to streak lines made by a neutrally buoyant dye when introduced at the same points into the flow. The fluid velocity vector is tangent to the streamline passing through a given point. We describe the observed airflow stream characteristics later. The nose is divided axially (along its long axis) into three regions: the vestibule and valve regions, the main (or central) nasal airway, and the nasopharynx. The overall flow profile is rendered in a highly simplified form in Figure 5.

In our descriptions that follow, the $+z$ coordinate axis is along the long axis of the nose and directed toward the nasopharynx, and this is referred to as the axial direction. The vertical direction is the y axis. The

RIGHTSLINK

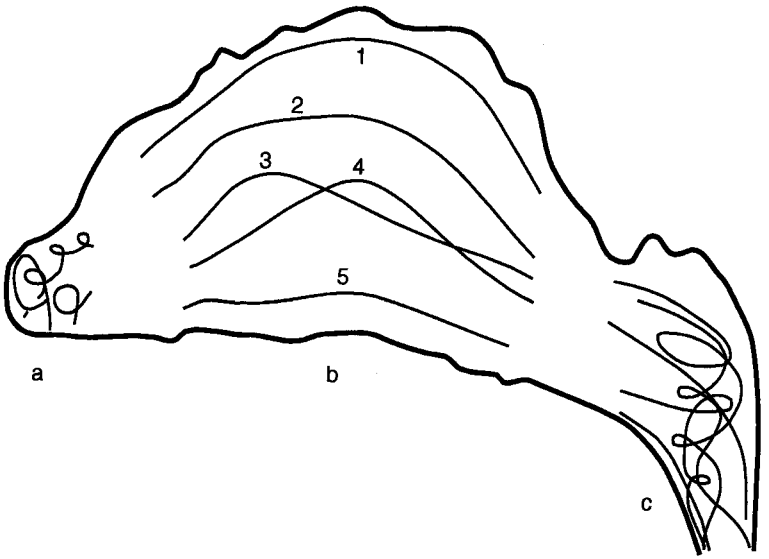

FIGURE 5. Representation of flow streamlines in (a) vestibule, (b) main airway, and (c) nasopharynx. Labels 1-5 refer to the dorsal, superior medial, middle medial, middle lateral, and ventral streams, respectively.

Inhalation Toxicology Downloaded from informahealthcare.com by University of Waterloo on 12/12/14
For personal use only.

coronal planes are perpendicular to the *z* axis, and the sagittal planes are parallel to the *y*-*z* plane.

Flow in the Nasal Vestibule and Valve Regions The simulated airflow pattern for the entire nose at the resting inspiratory rate of 15 L/min is represented in Figure 5. The nasal vestibule showed flow patterns that became increasingly complex as the inspiratory flow rate was increased. A recirculating stream was seen prominently in the left nasal vestibule (Figure 6a) but only weakly on the right side. A sagittal projection of the velocity vectors is shown in Figure 6c to further illustrate the flow confined to the recirculation zone. Streamlines originating in the most anterior portion of the nostril exhibited helical flow in the vestibule and in the anterior valve region. As a consequence of the helical flow, the speed associated with such streamlines decreased significantly. Masing (1967) injected dye in water flowing through a cast of the nose and observed swirling flow in laterally and ventrally flowing streams in the vestibule. Because of a low-lying nasal roof, the flow rising upward from the nostril was observed in our simulations to bend toward the floor as well as laterally. Ventrally flowing streams underwent strong lateral deflections in recesses along the nasal floor. The lateral as well as helical aspects of the flow led to secondary flow in the coronal planes. This feature of the flow can be seen from the streamlines in Figure 6b and is illustrated further in Figure 6d by projecting the air velocity vectors on a coronal plane in the vestibule.

RIGHTSLINK

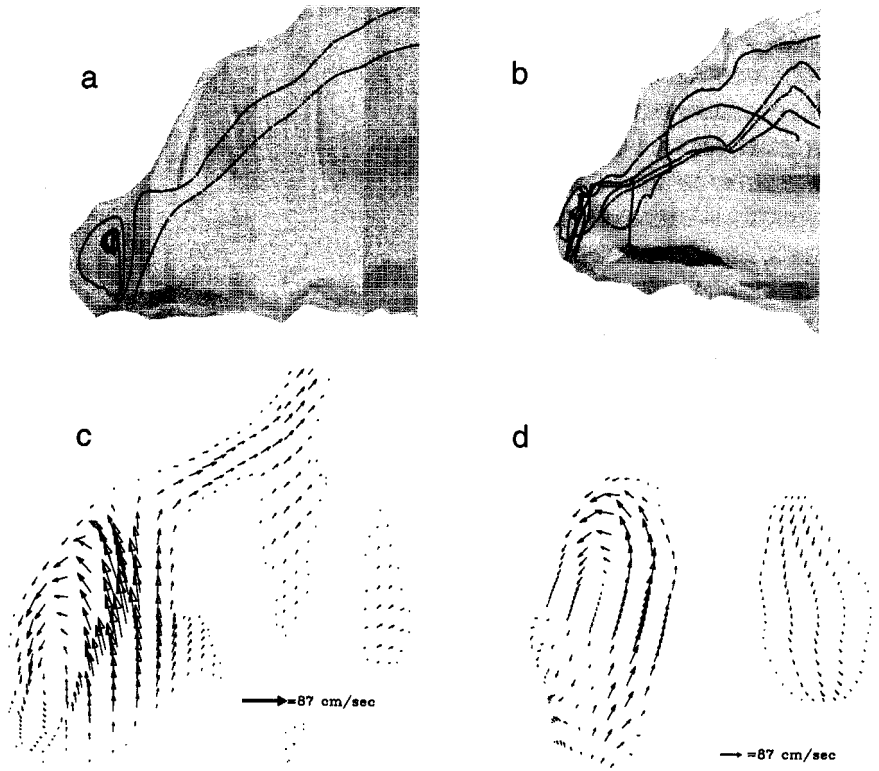

FIGURE 6. Flow in the nasal vestibule and nasal valve region. (a) Streamlines showing a zone of flow recirculation in the vestibule. (b) Streamlines showing helical flow. (c) Projection of velocity vectors along a sagittal plane. (d) Projection of velocity vectors along a coronal plane.

Flow in the Main Nasal Passages We classify the flow field in the main nasal passages into four main streams based on nasal anatomy as well as on the functional importance of regions through which the air streams flow. The nomenclature used for the streams can be understood by referring to Figure 3. The *medial* stream is comprised of flow through the middle medial and superior medial portion of the nose. The *ventral* stream passes through the inferior meatus and the inferior portions of the medial airway, thus flowing to a large extent close to the nasal floor, while the *lateral* stream comprises flow through the middle lateral, ventral lateral, and superior lateral portions of the inferior, middle, and superior meati. The *dorsal* stream flows vertically to the upper portions of the nose (through the dorsal airway), with a significant portion of the stream flowing through the olfactory region. Representative flow streams from these classifications (marked 1–5) are rendered in Figure 5 and further elaborated upon in Figure 7 (A–D). Where necessary for the discussion, these streams have been further subdivided (e.g., ventral lateral, superior medial) based on the portion of the airway that the stream was found to be flowing through.

Inhalation Toxicology Downloaded from informahealthcare.com by University of Waterloo on 12/12/14
For personal use only.

RIGHTSLINK

The origin of the medial stream (Figure 7A) was spread out over the inner regions of the nostril surfaces, with the superior portion of the stream originating from the anterior half of each nostril. Much of the medial stream was characterized by the airstream rising vertically from the nostril and subsequently bending 90 to 100 degrees at the vestibular roof toward the downstream direction. The superior medial stream and a portion of the inferior medial stream flowed largely perpendicular to the coronal planes in the anterior and central parts of the main nasal passages but were deflected laterally near the anterior nasopharynx. In this anterior nasopharyngeal region, the flow was nearly horizontal along axial planes transverse to the sagittal and coronal planes.

The ventral stream (Figure 7B) was the flow in the region below the inferior turbinate, through the inferior lateral meatus, and in the inferior portion of the airway between the inferior turbinate and the septum. Most of the ventral flow originated from the posterior portion of the nostrils, as was observed experimentally by Masing (1967), and along points close to the septal boundary. Further downstream, part of the stream that was ventral anteriorly rose vertically to flow through the middle lateral meatus.

Inhalation Toxicology Downloaded from informahealthcare.com by University of Waterloo on 12/12/14
For personal use only.

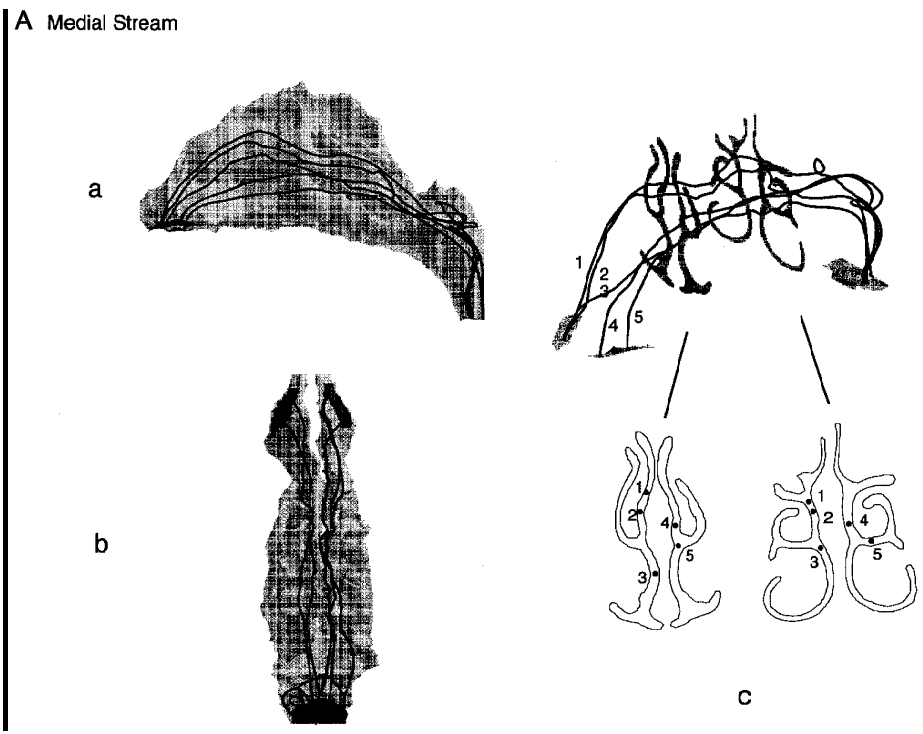

FIGURE 7. Simulated flow streamlines in the main nasal passages at 15 L/min showing (A) medial stream. Side (a), top (b), and oblique (c) views are presented. Viewing angle for the oblique display is along the $+x$, $+y$, $+z$ direction.

RIGHTSLINK

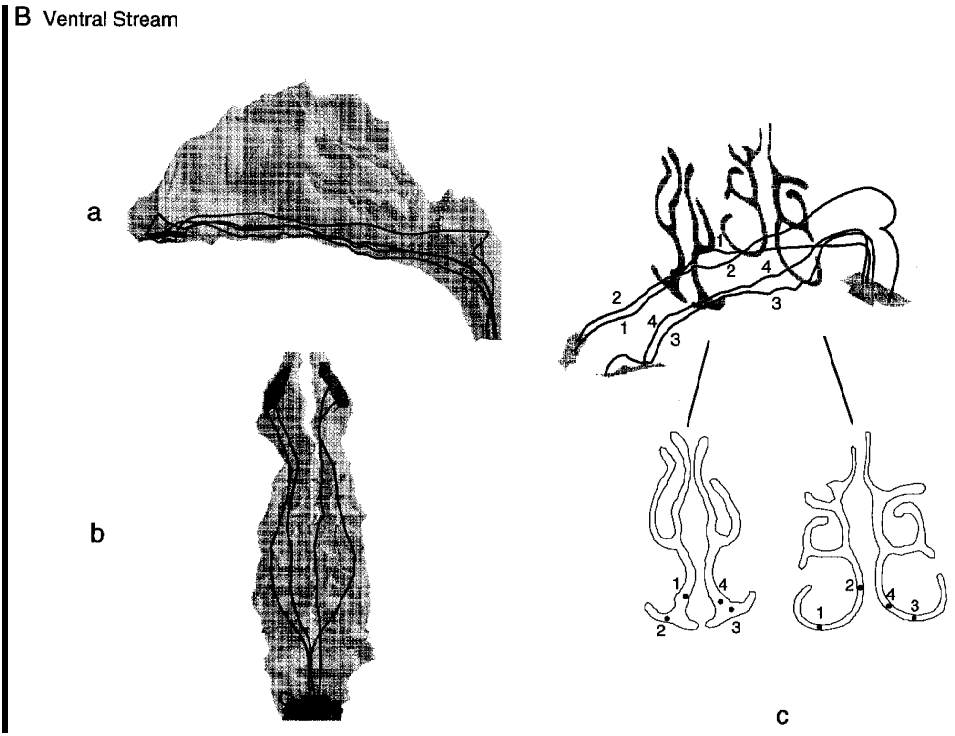

FIGURE 7. (*Continued*) Simulated flow streamlines in the main nasal passages at 15 L/min showing (B) ventral stream. Side (a), top (b), and oblique (c) views are presented. Viewing angle for the oblique display is along the $+x$, $+y$, $+z$ direction.

The ventral portion of the flow, like the dorsal, displayed considerable meandering, flowing medially in the anterior nose, and then through the inferior lateral meatus further downstream and deflecting again to the opposite side of the nasopharynx. Depressions on the nasal floor formed recesses, giving rise to small recirculating currents. In cases where streamlines originated near the septal boundary in the anterior portions of the nostril, the flow initially rose vertically, developing helical motion briefly before being deflected toward the floor.

The lateral stream (Figure 7C) originated along the lateral portions of the nostrils, rising vertically and undergoing deflection sideways to flow through the lateral middle meatus. The lateral streams meandered significantly, undergoing frequent changes in flow direction.

The dorsal stream (Figure 7D), which refers to flow to the upper regions of the nose, generally comprised the slowest flow in the main airway. The olfactory region in the human nose is located in the posterior dorsal portion of the main airway. While a significant portion of the dorsal stream flowed through the olfactory region, some of it turned downward after flowing anteriorly through the superior dorsal regions. Nearly

Inhalation Toxicology Downloaded from informahealthcare.com by University of Waterloo on 12/12/14
For personal use only.

RIGHTSLINK

all of the dorsal stream originated in the anterior portion of the nostrils, with some contribution to the flow from the middle portion of the left nostril. The projection of the dorsal airflow velocity along the coronal plane increased progressively posterior to the coronal section located midway in the main airway. The roof of the nose gradually lowers as the inhaled air approaches the nasopharynx from the main airway, thereby forcing the dorsal and superior medial airstreams downward.

Flow in the Nasopharynx Complex flow patterns were observed in the nasopharynx with downwardly spiraling, countercurrent vortices, as shown in Figures 5, 7, and 8. Vortex formation was prominent in the left nasal airway and weak in the right. This asymmetry is demonstrated in Figure 8, where the air velocity vector is projected on an axial section of the airway perpendicular to the sagittal and coronal planes (that is, on a plane perpendicular to the *y* axis). The vortex swirled clockwise (looking down) in the left side of the nose, and in an anticlockwise fashion in the right side.

A large portion of the middle medial and inferior medial streams flowed directly, after the initial change of direction in the vestibular area,

Inhalation Toxicology Downloaded from informahealthcare.com by University of Waterloo on 12/12/14
For personal use only.

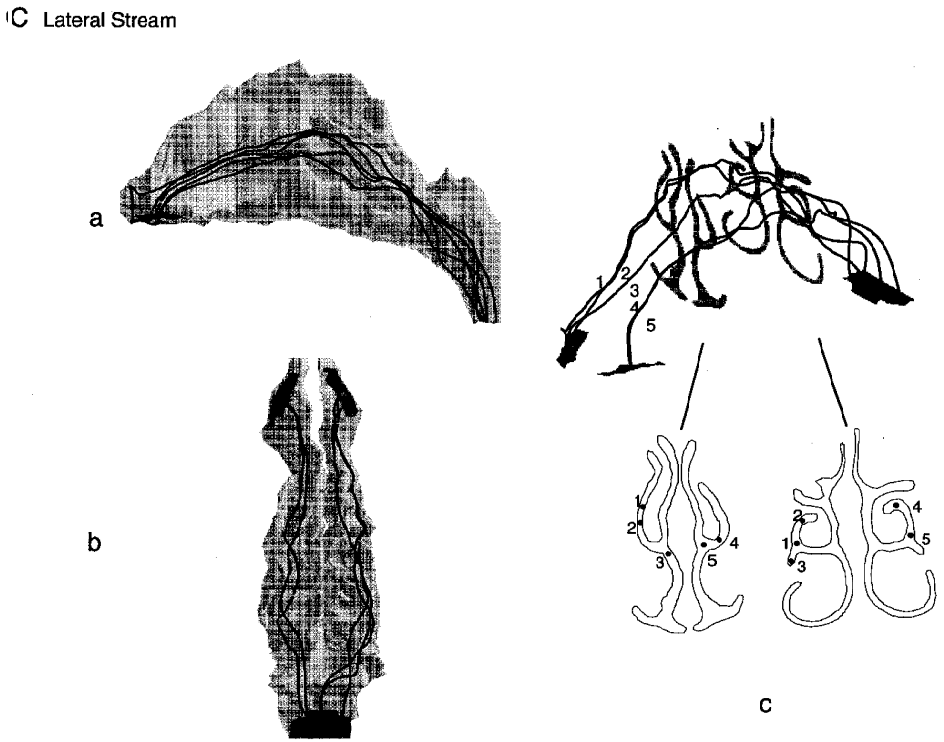

FIGURE 7. (*Continued*) Simulated flow streamlines in the main nasal passages at 15 L/min showing (C) lateral stream. Side (a), top (b), and oblique (c) views are presented. Viewing angle for the oblique display is along the $+x$, $+y$, $+z$ direction.

RIGHTSLINK

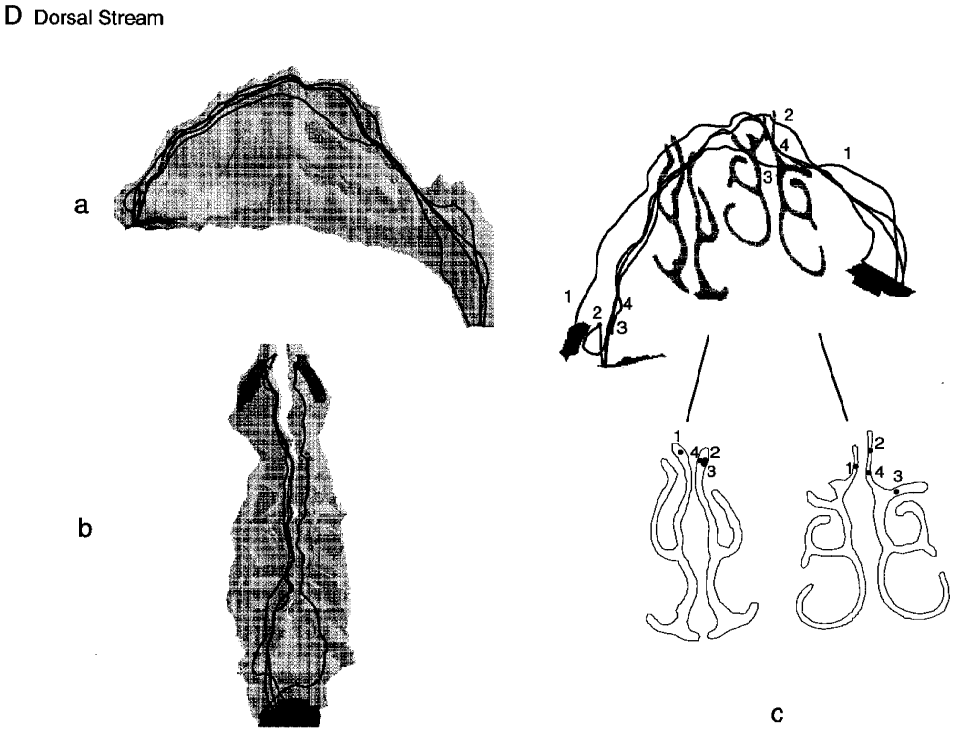

FIGURE 7. (*Continued*) Simulated flow streamlines in the main nasal passages at 15 L/min showing (D) dorsal stream. Side (a), top (b), and oblique (c) views are presented. Viewing angle for the oblique display is along the $+x$, $+y$, $+z$ direction.

Inhalation Toxicology Downloaded from informahealthcare.com by University of Waterloo on 12/12/14
For personal use only.

to the posterior nasopharynx without much change in flow direction or speed. In the nasopharynx, such streams flowed close and parallel to the posterior nasal wall. The nasopharyngeal region showed considerable crossover of flow between the two sides of the nose, as seen in Figures 7A, 7B, and 7D, for example. The axially directed middle stream from the right side flowed laterally in the anterior nasopharynx, exiting the nose through the right portion of the outlet. This crossing over was seen to occur much more frequently for streams originating in the right side of the nose.

Airflow Distribution

Figure 9 shows isospeed contour maps for the inspiratory flow rate of 15 L/min. The highest airspeed of 423 cm/s occurred in the posterior segment of the nasal valve region for airflow through the middle medial portion and was comparable with the peak speed for ventral flow through the same coronal section. The maximum speeds calculated at various coronal sections are shown for the inspiratory rate of 15 L/min in Table 1 with the location of the sections indexed in Figure 9. The first result at a distance of 3.3 cm from the anterior tip of the nose is at the posterior portion of the

RIGHTSLINK

nasal valve region, while all others pertain to the main nasal passages. The location at 7.8 cm was close to the anterior portion of the nasopharynx. The peak airspeed through any coronal slice of the main airway occurred either in the ventral or in the medial middle portion of the airway, with the highest airspeed occurring along the nasal floor. Airspeeds in the middle lateral meatus reached their peak (about three-fourths of the speed attained by the medial stream at the same axial distance) roughly halfway between the nostril and outlet, indicating that lateral flow in the nose was significant.

Examining regional volumetric flow distribution is useful since toxicological and clinical factors such as tissue susceptibility to pollutants and nasal resistance are site specific. Regional volumetric flow is determined by integrating the velocity component normal to a coronal plane over the cross-sectional area of various regions in the plane. This calculation was done for a coronal section at $z = 6$ cm, located in the posterior half of the main nasal passages. The partitioning of this section is shown in Figure 3, and results for airflow distribution for inspiratory flow rates of 15 L/min and 26 L/min are given in Table 2. The last column describes the flow apportionment as a percentage of the total flow through the entire coronal section.

The volumetric flow analysis provides the volume of air delivered per unit time to a lumen region, but it does not contain information on the extent of swirling or secondary flow that takes place. Since the main flow

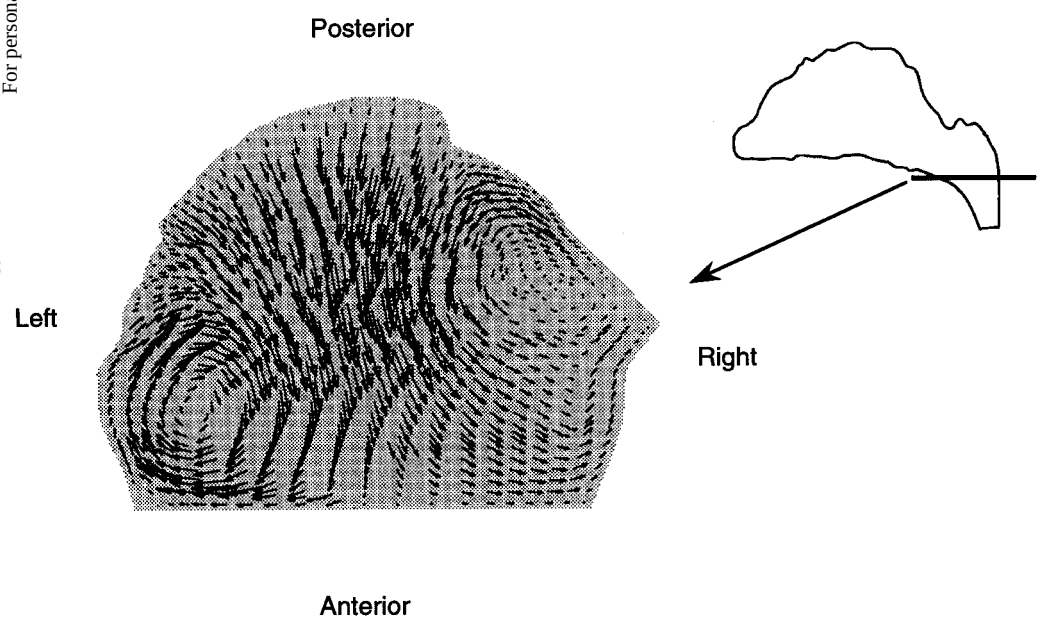

FIGURE 8. Projection of velocity vectors along an axial plane in the nasopharynx showing vortex flow.

Inhalation Toxicology Downloaded from informahealthcare.com by University of Waterloo on 12/12/14
For personal use only.

RIGHTSLINK

Inhalation Toxicology Downloaded from informahealthcare.com by University of Waterloo on 12/12/14
For personal use only.

FIGURE 9. Iso-speed contours for steady-state inspiratory flow rate of 15 L/min. The coronal planes on which the contour levels are plotted are viewed obliquely. The direction of main airflow is from left to right; nostril is to the left and outlet to pharynx is at the right end. The arrows indicate direction of flow, and indices a–e refer to sections in Table 1.

RIGHTSLINK

TABLE 1. Maximum airspeeds at various regions in the nose

Sections[b]	Axial distance, z[a] (cm)	Maximum airspeed (cm/s)		
		Medial stream	Ventral stream	Lateral stream
a	3.3	423	409	
b	4.1	314	389	
c	5.0	334	322	250 (Middle)
d	6.8	273	365	245 (Ventral)
e	7.8	259	210	

[a]Distance of coronal sections from the anterior end of the nose.
[b]Sections a–e through which the streams pass are indexed in Figure 9.

direction is not easily specified for complex geometries such as that of the nose, quantifying secondary flow is problematic albeit useful, as discussed later. Nevertheless, since flow in the main nasal passages is largely axial, the extent of swirling may be roughly assessed by comparing the z (axial) component of the velocity (u_z) with the magnitude of the velocity projected on the x-y (coronal) plane. This comparison is provided in Table 3, where we calculate regional averages of u_z, $(u_x^2 + u_y^2)^{1/2}$, and the speed $(u_x^2 + u_y^2 + u_z^2)^{1/2}$ for the same coronal section and inspiratory flow as shown for the volumetric flow rate in Table 2.

Error Analysis

The numerical stability of these results was characterized by examining the airflow speed and pressure at various points and volumetric flow

TABLE 2. Volumetric airflow distribution on coronal plane at z = 6 cm

Right nose				Left nose				Left + right nose, $Q/Q_{tot} \times 100$	
		Q (ml/s)				Q ml/s)			
Region	A (cm^2)	i = 15 L/min	i = 26 L/min	Region	A (cm^2)	i = 15 L/min	i = 26 L/min	i = 15 L/min	i = 26 L/min
A	0.079	2.1	4.0	A′	0.095	3.9	7.4	2.4	2.6
B	0.208	12.9	22.2	B′	0.238	15.9	27.5	11.5	11.5
C	0.154	2.1	3.5	C′	0.101	1.5	3.1	1.5	1.5
D	0.205	27.4	46.7	D′	0.255	37.0	63.4	25.7	25.5
E	0.343	25.8	43.8	E′	0.409	27.4	46.8	21.2	21.0
F	0.205	27.8	48.4	F′	0.214	34.6	58.4	24.9	24.8
G	0.289	15.8	27.4	G′	0.173	16.2	28.5	12.8	13.0

Note. A, cross-sectional area of airway. *Q,* volumetric flow over a cross-sectional area. Q_{tot}, total volumetric flow over the entire coronal section. *i,* inspiratory flow rate. The coronal plane at z = 6 cm is shown with the various regions of this table demarcated in Figure 3.

Inhalation Toxicology Downloaded from informahealthcare.com by University of Waterloo on 12/12/14
For personal use only.

RIGHTSLINK

TABLE 3. Average velocity components for airflow through coronal plane at $z = 6$ cm

Right nose							Left nose						
	$i = 15$ L/min			$i = 26$ L/min				$i = 15$ L/min			$i = 26$ L/min		
Region	u_z	u_p	u	u_z	u_p	u	Region	u_z	u_p	u	u_z	u_p	u
A	26.9	42.1	51.4	50.9	73.5	91.1	A′	41.2	63.9	77.8	77.8	119.9	146.0
B	62.0	42.5	77.6	106.6	73.0	133.2	B′	66.8	34.7	79.9	115.8	67.4	142.3
C	13.8	18.5	23.9	22.4	29.1	38.0	C′	15.0	14.7	21.3	30.4	31.6	44.4
D	134.0	23.8	136.6	228.3	42.6	233.3	D′	145.2	27.5	149.3	248.7	48.7	256.3
E	75.4	66.5	102.7	127.9	114.4	175.3	E′	66.9	43.6	81.3	114.3	74.6	139.2
F	135.8	21.2	138.6	236.8	37.0	241.4	F′	162.1	23.4	164.8	273.6	40.4	278.2
G	54.5	54.7	79.1	94.9	94.2	137.2	G′	93.8	49.5	107.4	164.8	87.8	189.3

Note. The following quantities are averaged over various regions on the plane: (1) the axial component of the velocity, u_z; (2) the magnitude of the projection of the velocity along the coronal (x–y) plane, $u_p = (u_x^2 + u_y^2)^{1/2}$; (3) the speed $(u = u_x^2 + u_y^2 + u_z^2)^{1/2}$. The averaged values are tabulated for inspiratory flow rates, i, of 15 L/min and 26 L/min. Regions indicated in this table are demarcated in Figure 3. See Table 2 for areas of regions. Units are in cm/s except where otherwise indicated.

Inhalation Toxicology Downloaded from informahealthcare.com by University of Waterloo on 12/12/14
For personal use only.

for various regions for three different mesh densities. The mesh densities used were 156K nodes, 124K nodes, and 86K nodes. The discrepancies in volumetric flow ranged from 0 to 9% of the result obtained with the densest mesh. The differences in the nodal values (of speed and pressure) generally ranged from 3 to 10% of the result obtained with the densest mesh, except for a few points that had discrepancies ranging from 10 to 20% in the nodal values. The results reported in this work were obtained using the mesh of 156K nodes.

Comparison with Experiment

Calculated results of air velocity in the nasal passages were compared with hot-wire anemometry measurements of the axial component (u_z) of the velocity made by Hahn et al. (1993) in an enlarged nasal model. Because the nasal model used in the experiment terminated at the anterior nasopharynx, velocities in the nasopharynx were not compared in this experiment. We have used the values measured by Hahn et al., as presented in the study by Keyhani et al. (1995), for the purpose of comparison.

A comparison between simulation and experiment for u_z plotted as a function of distance from the lateral wall of the nose (measured as a fraction of the airway width) is shown in Figure 10, 1–8. Locations of the measurements are given in Figure 2A. Peaks in the velocity, which occurred at the central portions of the airway, are in good agreement (within 5%) with the experiment in plots 1, 3, 5, 6, and 7, within 25% of the experimental value in plots 2 and 4, and within 35% in plot 8. The

RIGHTSLINK

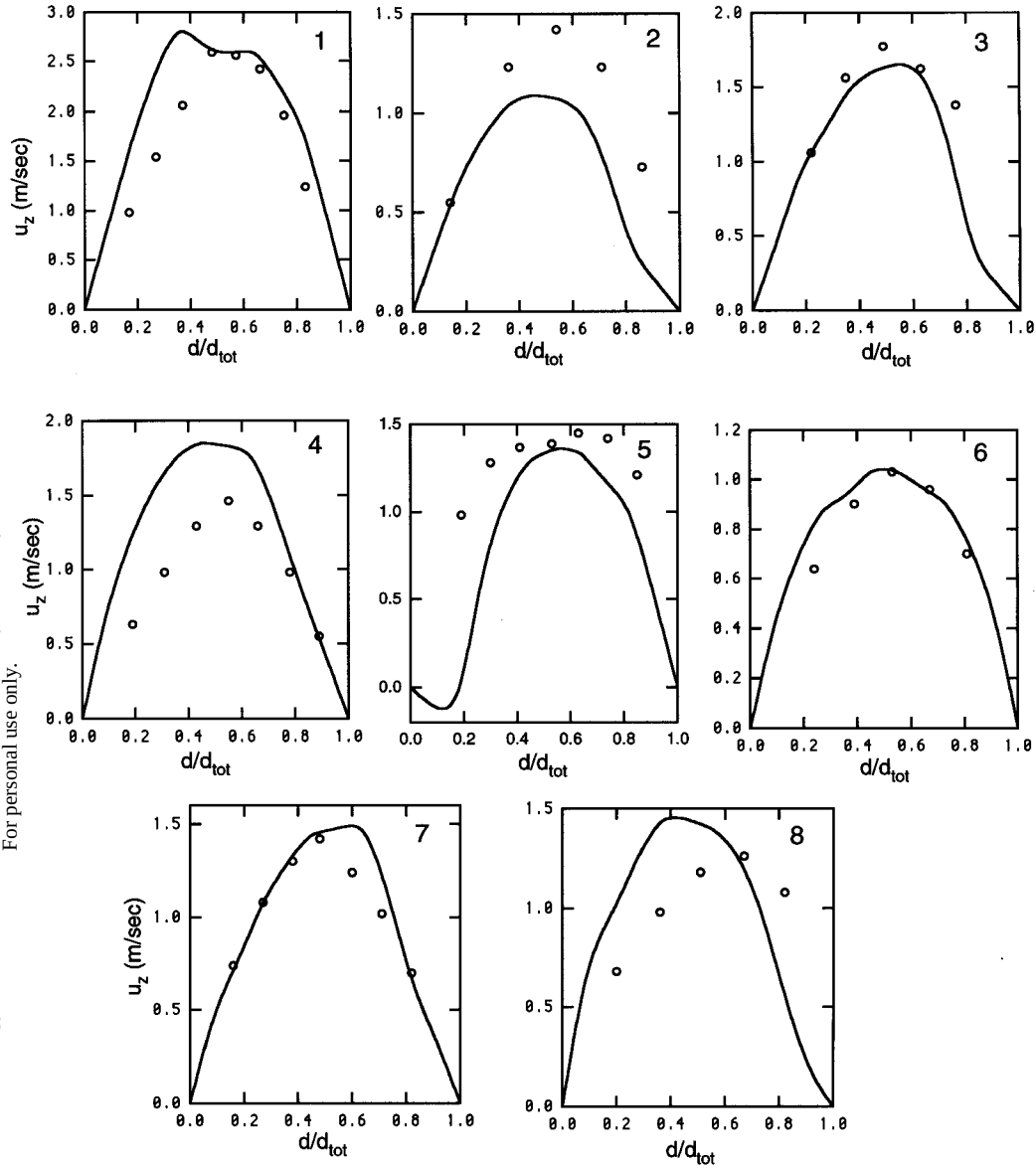

FIGURE 10. Comparison of axial component of velocity (u_z). Numerical results are shown by lines and experimental results by circles. The experimental values are those measured by Hahn et al. (1993) but reproduced in the format presented here from Keyhani et al. (1995). See Figure 2A for details on the location where measurements were made. d, Distance from lateral wall; d_{tot}, width across one side of the airway (along the solid line in Figure 2A).

Inhalation Toxicology Downloaded from informahealthcare.com by University of Waterloo on 12/12/14
For personal use only.

RIGHTSLINK

range of disagreement with experimental value is much greater, ranging from 5 to 70% of the experimental value, as the location of measurement moves closer to the airway wall.

The pressure drop across the nasal cavity between the nostril opening and the outlet was 32 Pa at the inspiratory rate of 15 L/min. This pressure drop compares with the value of 55 Pa derived from Figure 7 of the report by Schreck et al. (1993) of measurements in a cast of the human nose but is significantly less than the average clinical value* of 110 ± 62.5 (SD) reported by Hirschberg et al. (1995) in plethysmograph measurements on normal male adults. The wide range of values seen in the preceding clinical measurements points to large intersubject variations and highlights concerns in comparing results on differing nasal geometries. Since our result is within 1.3 standard deviations of the average clinical result, it is possible that the discrepancy of simulation both with the values of Schreck et al. and with that of Hirschberg et al. may be due to statistical variability.

DISCUSSION

The purposes of the numerical simulations in this work were (1) to determine the airflow profile in human nasal passages at resting and light exercise steady-state inspiration and correlate the flow characteristics with the complex geometry of the nasal passages, and (2) to determine whether CFD simulations of the airflow profile agreed with laboratory experiment.

The airflow streams may be qualitatively summarized as complex (with strong secondary components) in the anterior and posterior regions of the nose, while largely streamlined and smooth in the main nasal passages. Within the numerical limits of the computational grid used in this simulation, the airflow appears to be laminar at the inspiratory rates of 15 L/min and 26 L/min. These conclusions are in agreement with the results of studies by Keyhani et al. (1995) and Hahn et al. (1993) but contrast with Swift and Proctor (1977) for the higher inspiratory flow rate. Swift and Proctor used a miniature Pitot device to measure airflow velocity and made visual observations of dye streamlines in water flow through a nasal cast. At a flow rate dynamically similar (see Hahn et al., 1993) to a full nasal airflow rate of 15 L/min, they concluded the flow to be laminar, but at 25 L/min, the flow turned turbulent posterior to the nasal valve. A similar conclusion was reached by Schreck et al. (1993), who observed flow separation in the dorsal portion of the nose near the nasal valve region, a likely consequence of the sudden expansion, downstream of the vestibule, in the nasal airway geometry used in their model.

In the present study, the recirculating flow observed in the vestibule is a consequence of an abrupt change in the slope of the nasal roof rising

*In arriving at this value, we used their published result for the average nasal resistance measured in 30 normal adults and the unpublished communication that the measurements were performed at an inspiratory flow rate of 15 L/min.

Inhalation Toxicology Downloaded from informahealthcare.com by University of Waterloo on 12/12/14
For personal use only.

RIGHTSLINK

vertically upward from a nearly horizontal orientation (roughly parallel to the nostril surface) in the anterior region. Helical and swirling flow in the vestibule led to considerable decrease in the speed (up to 60% of that at the inlet) of a portion of the flowstream in the vestibule. Less than 1 cm further downstream, the highest airspeeds in the nose (up to 420 cm/s) were attained in the posterior nasal valve region, where the coronal cross-sectional area is small. These features of airflow in the anterior nose indicate that nasal resistance may be altered significantly by changes to the airway geometry in this region, as is also evident from the finite-element study by Tarabichi and Fanous (1993). Streamlines undergoing helical flow in the healthy human nose originate in the anterior portion of the nostril with a significant portion leading into the olfactory region further downstream; therefore increased dissipation of this flow could adversely affect olfaction. Studies of airflow in the upper respiratory tract may thus be a valuable tool to accompany traditional otolaryngological diagnosis.

Vortex formation in the nasopharynx is a consequence of the pattern of merging of left and right airways. At this location, the fused airways expand vertically in the medial region and laterally in the dorsal and middle portions with a shrinking of the lateral ventral segment. The expansion results in the formation of high-pressure zones in the superior lateral portions of the nasopharynx accompanied by a relatively low pressure in the mid portions of the nasopharynx and an axial pressure gradient that is reverse to the direction of main flow. The downward-spiraling vortices that develop as a consequence are, however, asymmetric between the right and left sides. Air from the right was observed to feed laterally into the vortex on the left side, significantly weakening the vortex formation in the right nasopharynx. Such an asymmetry may be better understood by correlating the flow with the pressure profile. The high pressure in the right side of the superior lateral nasopharynx is higher than the pressure in the corresponding zone on the left, while in the vertical direction the drop in pressure on the right side is less than that on the left. These and other differences in flow patterns in the two sides of the nose may be partly a consequence of nasal cycling and are therefore likely to change depending upon the time at which the MRI scanning of the subject was done with respect to the cycle. Swift and Proctor (1977) indicate that the turbulence they observed in airflow through the main nasal passages (at 25 L/min) is reduced at the nasopharynx. Our results suggest the contrary, namely, that if turbulent flow occurs the vortices are likely to add to the instability.

Our finding that the olfactory stream originates in the anterior portion of the nostril surface is in agreement with a similar conclusion by Keyhani et al. (1995) and the experimental observation of Hahn et al. (1993). This finding is in contrast, however, with earlier data in the literature. The medial and central portions of the nostril were found to be responsible by Masing (1967) for directing an aqueous suspension of alu-

Inhalation Toxicology Downloaded from informahealthcare.com by University of Waterloo on 12/12/14
For personal use only.

RIGHTSLINK

minum particles to the olfactory region. Hornung and colleagues (1987), on the other hand, found that radioactive gas was directed to the same region by the lateral portion of the nostrils. These variations are probably due to interindividual differences in anatomy and differences between in vivo and cadaver nasal anatomies. Hornung et al. and Masing used nasal models prepared from a human cadaver, whereas the model of Hahn (identical to that of Keyhani) and the model presented here are based on computerized axial tomography (CAT) and MRI scans, respectively, of healthy adult noses.

Results for the axial velocity in the central portions of the airway, located midway between the nasal walls for a particular coronal section in Figure 10, are generally in good agreement (within 5–25% of the experimental value), with those obtained in the Hahn et al. (1993) experiment. This observation indicates that the core portion of the flow has been accurately described by the simulation. The experiment and our simulation pertained to different noses, but the overall nasal geometries were generally similar, allowing for a comparison of results. The differences in the above peak velocities, measured at the central portions of the airway, could be due to variations in the shapes of the nasal passages of two different individuals. This is evident for the measurement in plot 2 of Figure 10—the dorsal portion of the main nasal airway in the Hahn et al. experiment was significantly shorter and wider than in the nose used in our model. The lack of agreement (35%) in the peak axial velocities in plot 8 of Figure 10 may be due to the termination of the experimental model at the coronal section at which this measurement was made, therefore subjecting the flow to artificial constraints (see Figure 2A, part e).

We believe that larger differences between experimental measurements and the simulations presented here for locations close to the nasal walls, ranging from less than 5% up to 70% of the experimental value, are due to a combination of experimental and numerical errors. The experimental errors were assessed to be mainly related to natural convection effects induced by the hot probe. These effects were more pronounced at the lower velocities closer to the walls and in the positioning of the sensor probe (Keyhani et al., 1995; Hahn et al., 1993). Numerical errors in velocities simulated close to the nasal airway walls could originate from the lack of a higher density of grid points near the walls. The lack of a grid with such a differentially graded spacing is one of the limitations of the present study. Thus, closer to the nasal lining, the agreement of the model with experiment is encouraging but not conclusive.

The maximum airspeed and the location at which it occurred in our simulation were in good agreement with those calculated by Keyhani et al. (1995) (4 m/s) for the same nasal geometry as used in the experiment discussed earlier and is in the anterior region of the nose (z = 3.3 cm). The location of this maximum is in the middle medial airway, but our simulated airspeed along the nasal floor (the region where Keyhani's max-

Inhalation Toxicology Downloaded from informahealthcare.com by University of Waterloo on 12/12/14
For personal use only.

RIGHTSLINK

imum occurs) is lower than that in the middle medial by only 3%. Based on the results in Table 1, we conclude that the highest airspeeds are equally likely to occur in the middle medial or in the ventral airway of the nose. Airspeeds throughout the olfactory region of the airway are among the lowest in the nose, as also observed in the Keyhani study; the average speed through the olfactory region at z = 6 cm in the present study was 62 cm/s, at the flow rate of 15 L/min.

The examination of numerical stability in the results leads us to expect that values of variables averaged over a sizeable region, such as volumetric flow, will not change appreciably with further refinements of the mesh used in this simulation. However, there were regions in the finite-element mesh where values of the velocity and pressure variables evaluated at the nodes of the finite-element mesh showed significant differences with the two mesh refinements. The differences between the results obtained using meshes of 156K nodes and 124K nodes were not generally less than the discrepancy between those obtained using meshes of 86K nodes and 124K nodes. It is therefore reasonable to expect some mesh dependency in results for nodal values (such as speed contours and streamlines) reported in this article using the mesh of 156K nodes. Mesh refinements are accompanied by large increases in computational requirements; therefore an assessment of whether a more refined study is to be made hinges on the quantity being calculated for a specific application. Because results with the densest mesh were in good general agreement with experimental measurements, results generated using the densest mesh were considered adequate with regard to accuracy.

The volumetric flow analysis (shown in Table 2 for the coronal section at z = 6 cm) shows that the stream passing through the middle medial airway and ventral medial airway delivers, volumetrically, the largest proportion (26% and 25%, respectively) of air, with the highest air speeds occurring in these regions. The results suggest a larger delivery of pollutants along the middle and ventral medial airways, thus placing the medial portion of the middle medial and inferior turbinates at a higher risk of exposure. This conclusion is consistent with the finding that the anterior middle turbinate forms a preferential area for dust particle deposition (Torjussen, 1983) and is the site of nasal carcinomas in nickel-exposed workers (Virtue, 1972) as well as of human nasal lesions in general (Scherer et al., 1996). In studies of airflow in the rat nose previously carried out in this laboratory, the areas through which volumetric flow was highest were seen to correlate with regions most prone to lesions due to exposure to reactive and water-soluble chemicals such as formaldehyde (Morgan et al., 1991). Nasal airflow distribution along with information on tissue susceptibility may therefore be a predictor of toxic response for those chemicals and particles for which uptake is largely determined by the air-phase delivery of the inhaled toxicant to the nasal surface.

There was almost no change in flow apportionment to different

Inhalation Toxicology Downloaded from informahealthcare.com by University of Waterloo on 12/12/14
For personal use only.

RIGHTSLINK

regions as the inspiratory flow rate increased from the resting inspiratory rate of 15 L/min to 26 L/min, that of light exercise (Table 2), in agreement with similar conclusions reached in both the Hahn et al. experiment (1993) and the simulation by Keyhani et al. (1995). The lateral portion of the middle airway receives a large fraction of the flow (21%), higher than the 8.5% reported in the Keyhani study. Most of the lateral flow in their simulation appears to occur ventrally at this coronal section (29.5%), twice the corresponding flow that we obtained.

On the other hand, the olfactory region receives only a small portion (2.4%) of the flow in our simulation. As seen in the case of the axial velocity, this result is in disagreement with that of Keyhani et al. (1995), who report a threefold higher percentage of flow to the olfactory region at the same coronal cross section. The dorsal airways reconstructed in the present study are more narrow than those in the Keyhani study, which could account for the observed difference. In both models, dorsal airway widths are much narrower than those elsewhere in the nasal passages, resulting in increased resistance to airflow in the downstream direction. A portion of the flow is channeled downward along the path of least resistance, continually depleting delivery of the dorsal stream to the olfactory region. This effect is seen in Table 3, where in the olfactory region the average magnitude of the velocity projected on a coronal plane is considerably greater than the component perpendicular to the plane. A large secondary-to-axial flow ratio extends down to nearly the upper one-half of the airway at $z = 6$ cm. The middle medial and ventral medial flow here is almost completely axial, but the axial component is comparable to the secondary component for the middle lateral and ventral lateral flow. In general, the flow profile shows a significant lateral component of flow, as may be seen from Table 3 and Figure 9.

While the overall qualitative features of the flow were similar between the two sides of the nose, there were quantitative differences, as is to be expected from differences seen in the shapes of the coronal sections and the nostril openings on either side. This asymmetry in flow profiles may be assessed from the data in Tables 2 and 3. For flow through the coronal section at $z = 6$ cm, the volumetric flow through the left side was greater than that through the right by a factor of 1.2, equal to the ratio of the surface areas of the left and right nostrils. For this coronal section, the average velocity was higher in the left nose for the dorsal and medial streams, with the difference ranging from a factor of 1.2 to 1.8. The lateral stream, on the other hand, flowed faster by a factor of up to 1.5 in the right nose. The difference between the secondary and axial velocity components of the medial streams, discussed earlier as averages over the left and right sides, remained roughly unchanged when the quantities were separately averaged over each side of the nose. For the lateral streams (the superior and ventral components), the speed averaged over the corresponding regions on the section (Table 3) was significantly higher on the right side than on the left.

Inhalation Toxicology Downloaded from informahealthcare.com by University of Waterloo on 12/12/14
For personal use only.

RIGHTSLINK

Inhalation Toxicology Downloaded from informahealthcare.com by University of Waterloo on 12/12/14
For personal use only.

In the main nasal airway, the middle medial and ventral medial airstreams possessed the highest speeds as well as flow without significant reduction in speed. The nasopharynx, located directly in the path of these streams, is also therefore a potential hot spot for the effects of airborne toxicants. The "impacting" nature of flow in the nasopharynx has also been discussed by others (Proetz, 1951; Swift & Proctor, 1977) and is associated with thinning of the wall boundary layer due to the abrupt change in the direction of the main flow stream. The posterior nasopharyngeal wall, perhaps not coincidentally, is lined with protective lymphoid tissue and pit-like particle-trapping structures (crypts) that are washed by the mucociliary stream (Swift & Proctor, 1977). Vortex formation in the nasopharynx and flow recirculation in the vestibule will lead to increased residence times in these zones, thereby affecting diffusion and exchange of gas molecules through the nasal lining.

Various approximations were employed in this model, the most notable of which is the assumption of a steady-state inspiratory condition. The validity of using such an approximation can be estimated by the Strouhal number or frequency parameter, $S = \omega L/u$, where ω, L, and u are the breathing frequency, axial length of the nasal airway, and the average velocity, respectively. The value of S is 0.02 for a resting breathing frequency, $\omega = 0.25$ Hz, $L = 11$ cm, and $u = 144$ cm/s, corresponding to a flow rate of 26 L/min and a cross-sectional area of 3 cm^2. Unsteady effects may be considered insignificant when the frequency parameter is less than 1 (Pedley et al., 1977). Expiratory flow patterns can be expected to be significantly different from those obtained for the inspiratory case, as can be observed from the studies by Keyhani et al. (1995) and Hahn et al. (1993). Thermal effects were ignored, based on the conclusion of Keyhani et al. that these effects are negligible.

The assumption of rigid nasal walls precludes the occlusion of airways that occurs because of nasal cycling as well as the large changes that occur during nasal collapse and oronasal partitioning of airflow. The latter effects, however, occur normally only at much higher inspiratory rates (such as during vigorous sniffing or heavy exercise) than the resting inspiratory rates considered in this work. At these higher flow rates, conditions that model a moving boundary will need to be imposed on the nasal walls and a time-dependent simulation carried out. At such flow rates, a turbulent flow scenario is also to be expected. In order to be most effectively and widely used as a tool, the CFD model development will need to incorporate interindividual variations in nasal anatomy. Efforts in this direction are underway (Brin et al., 1997).

Simulations of nasal airflow may be used in various applications. Of particular importance is the potential use of CFD models of airflow as a critical component in assessing human risk from exposure to inhaled chemicals. Most health effects data are obtained from studies using laboratory animals because a wide array of endpoints and invasive procedures can be used. Toxicology is becoming an increasingly mechanistic and quantitative

RIGHTSLINK

endeavor. Relative to the respiratory tract, site-specific dose and response results in animals are available for assessing potential human risks, and there has been a particularly increased interest in recent years in the nasal toxicity and dosimetry of inhaled chemicals (Miller, 1995).

Quantitative assessments of risk involve interspecies extrapolations of dose. By using CFD models of airflow in laboratory animals in conjunction with algorithms to determine the flux of the chemical into the airway epithelium, the local tissue doses associated with effects in animal studies can be compared with tissue doses that human airflow and flux models indicate to be likely associated with human exposure scenarios. We are currently using the CFD models presented in this work in projects to extrapolate the dose of xenobiotics associated with tissue lesions in laboratory animals to human exposure levels. Use of the CFD model reduces uncertainties in human health risk assessments by (1) providing site-specific dosimetric information and (2) specifically considering complex nasal anatomy in extrapolation of the highly unevenly distributed dose from animals to humans. These factors are not considered in current default methodologies for risk assessment.

Inhalation Toxicology Downloaded from informahealthcare.com by University of Waterloo on 12/12/14
For personal use only.

REFERENCES

Andersen, I., and Proctor, D. F. 1982. The fate and effects of inhaled materials. In *The nose, upper airway physiology and the atmospheric environment,* eds. D. F. Proctor and I. Andersen, pp. 423–455. New York: Elsevier Biomedical Press.

Bridger, G. P., and Proctor, D. F. 1970. Maximum nasal inspiratory flow and nasal resistance. *Ann. Otol. Rhinol. Laryngol.* 79:481–488.

Brin, L., Huband, J., Miller, J., Potter, L. K., Price, M., Kimbell, J. S., and Kepler, G. M. 1997. Shape-based mathematical modeling of the human nasal passages. *Proceedings, NCSU 1996 Industrial Mathematics Modeling Workshop For Graduate Students,* CRSC-TR97-8 37-66.

Cole, P. 1982. Upper respiratory airflow. In *The nose, upper airway physiology and the atmospheric environment,* eds. D. F. Proctor and I. Andersen, pp. 163–183. New York: Elsevier Biomedical Press.

Cole, P. 1993. *The respiratory role of the upper airways.* St. Louis, MO: Mosby Year Book.

Elad, D., Liebenthal, R., Wenig, B. L., and Einav, S. 1993. Analysis of airflow patterns in the human nose. *Med. Biol. Eng. Comput.* 31:585–592.

Fluid Dynamics International. 1991. *FIDAP. Fluid dynamics analysis package: Theory manual.* Evanston, IL: Fluid Dynamics International (now Fluent Inc., Lebanon, NH).

Fluid Dynamics International. 1996. *FIDAP. Fluid dynamics analysis package: User's manual.* Evanston, IL: Fluid Dynamics International (now Fluent Inc., Lebanon, NH).

Frederick, C. B., Morris, J. B., Kimbell, J. S., Morgan, K. T., and Scherer, P. S. 1994. Comparison of four biologically based dosimetry models for the deposition of rapidly metabolized vapors in the rodent nasal cavity. *Inhal. Toxicol.* 6(suppl.):135–157.

Girardin, M., Bilgen, E., and Arbour, P. 1983. Experimental studies of velocity fields in a human nasal fossa by laser anemometry. *Ann. Otol. Rhinol. Laryngol.* 92:231–236.

Godo, M. N., Morgan, K. T., Richardson, R. B., and Kimbell, J. S. 1995. Reconstruction of complex passageways for simulations of transport phenomena: Development of a graphical user interface for biological applications. *Comp. Meth. Prog. Biomed.* 47:97–112.

Guilmette, R. A., Cheng, Y. S., Yeh, H. C., and Swift, D. L. 1994. Deposition of 0.005–12 μm monodisperse particles in a computer-milled MR-imaging based nasal airway replica. *Inhal. Toxicol.* 6(suppl. 1):395–399.

RIGHTSLINK

Hahn, I., Scherer, P. W., and Mozel, M. M. 1993. Velocity profiles measured for airflow through a large-scale model of the human nasal cavity. *J. Appl. Physiol.* 75:2273–2287.

Haight, S. J., and Cole, P. 1983. Site and function of the nasal valve. *Laryngoscope.* 93:49–55.

Hirschberg, A., Roithmann, R., Parikh, S., Miljeteig, H., and Cole, P. 1995. The airflow resistance profile of healthy nasal cavities. *Rhinology* 33:10–13.

Hornung, D. E., Leopold, D. A., Youngentob, S. L., Sheehe, P. R., Gagne, G. M., Thomas, F. D., and Mozell, M. M. 1987. Airflow patterns in a human nasal model. *Arch. Otolaryngol. Head Neck Surg.* 113:169–172.

International Commission on Radiological Protection. 1975. *Report on the task group on Reference Man.* Oxford: Pergamon Press.

Keyhani, K., Scherer, P. W., and Mozell, M. M. 1995. Numerical simulation of airflow in the human nasal cavity. *J. Biomech. Eng.* 117:429–441.

Kimbell, J. S., Gross, E. A., Joyner, D. R., Godo, M. N., and Morgan, K. T. 1993. Application of computational fluid dynamics to regional dosimetry of inhaled chemicals in the upper respiratory tract of the rat. *Toxicol. Appl. Pharmacol.* 121:253–263.

Lang, J. 1989. *Clinical anatomy of the nose, nasal cavity and paranasal sinuses.* New York: Thieme Medical.

Lanza, D. C., and Clerico, D. M. 1995. Anatomy of the human nasal passages. In *Handbook of olfaction and gustation,* ed. R. L. Doty, pp. 53–73. New York: Marcel Dekker.

Masing, H. 1967. Expermentelle untersuchungen über den strömungsverlauf im nasenmodell. *Arch. Klin. Exp. Ohren. Nasen Kehlkopfheilk* 189:371–381.

Miller, F. J., ed. 1995. *Nasal toxicity and dosimetry of inhaled xenobiotics.* Washington, DC: Taylor & Francis.

Morgan, K. T., and Monticello, T. M. 1990. Airflow, gas deposition, and lesion distribution in the nasal passages. *Environ. Health Perspect.* 85:209–218.

Morgan, K. T., Kimbell, J. S., Monticello, T. M., Patra, A. L., and Fleishman, A. 1991. Studies of inspiratory airflow patterns in the nasal passages of the F344 rat and rhesus monkey using nasal molds: Relevance to formaldehyde toxicity. *Toxicol. Appl. Pharmacol.* 110:223–240.

Negus, V. 1958. *The comparative anatomy and physiology of the nose and paranasal sinuses.* London: Livingstone.

Olsen, J. H., and Asnaes, S. 1985. Formaldehyde and the risk of squamous cell carcinoma of the sinonasal cavities. *Br. J. Ind. Hyg.* 43:769–774.

Pedley, T. J., Schroter, R. C., and Sudlow, M. F. 1977. Gas flow and mixing in airways. In *Bioengineering aspects of the lung,* ed. J. B. West, pp. 229–233. New York: Marcel Dekker.

Proctor, D. F. 1982. The upper airway. In *The nose, upper airway physiology and the atmospheric environment,* eds. D. F. Proctor and I. Andersen, pp. 23–43. New York: Elsevier Biomedical Press.

Proetz, A. W. 1951. Air currents in the upper respiratory tract and their clinical importance. *Ann. Otol. Rhinol. Laryngol.* 60:439–467.

Roush, G. C., Walrath, J., Stayner, L. T., Kaplan, S. A., Flannery, J. T., and Blair, A. 1987. Nasopharyngeal cancer, sinonasal cancer, and occupations related to formaldehyde: A case-control study. *JNCI* 79(6):1221–1224.

Scherer, P. W., Yang, C. G., and Keyhani, K. 1996. Finite element modeling of gaseous pollutant uptake in the human nasal cavity. *Ann. Biomed. Eng.* 24(suppl. 1):S–80.

Schreck, S., Sullivan, K. J., Ho, C. M., and Chang, H. K. 1993. Correlations between flow resistance and geometry in a model of the human nose. *J. Appl. Physiol.* 75:1767–1775.

Subramaniam, R. P., Morgan, K. T., and Kimbell, J. S. 1996. Modeling airflow in the upper respiratory tract: Delivery of xenobiotics to the nasopharynx. *Ann. Biomed. Eng.* 1996. 24(suppl.): S–82.

Swift, D. L., and Proctor, D. F. 1977. Access of air to the respiratory tract. In *Respiratory defense mechanisms,* eds. J. D. Brain, D. F. Proctor, and L. M. Reid, pp. 63–91. New York: Marcel Dekker.

Tarabichi, M., and Fanous, N. 1993. Finite element analysis of airflow in the nasal valve. *Arch. Otolaryngol. Head Neck Surg.* 119:638–642.

Inhalation Toxicology Downloaded from informahealthcare.com by University of Waterloo on 12/12/14
For personal use only.

RIGHTSLINK

Torjussen, W. 1983. Nasal cancer in nickel workers. Histopathological findings and nickel concentrations in the nasal mucosa of nickel workers, and a short review of chromium and arsenic. In *Nasal tumors in animals and man: Tumor pathology,* eds. G. Reznik and S. F. Stinson, pp. 33–53. Boca Raton, FL: CRC Press.

Virtue, J. A. 1972. The relationship between the refining of nickel and cancer of the nasal cavity. *Can. J. Otolaryngol.* 1:37.

Vogel, S. 1994. *Life in moving fluids,* 2nd ed. Princeton, NJ: Princeton University Press.

Zienkiewicz, O. C. 1977. *The finite element method,* 3rd ed. London: McGraw-Hill.

Inhalation Toxicology Downloaded from informahealthcare.com by University of Waterloo on 12/12/14
For personal use only.

RIGHTSLINK